Ionized molecular hydrogen build-up and confinement inside the space charge of a continually resupplied electron cloud

A. S. Kiester, C. A. Ordonez, D. L. Weathers

Department of Physics, University of North Texas, 1155 Union Circle, #311427, Denton TX 76203, United States

Abstract—A cylindrically symmetric electromagnetic ion trap has been constructed that creates a potential well suitable for confining ions with the space charge of a continually resupplied electron cloud. The trap uses permanent magnets to form a linear array of magnetic field ring cusps in a cylindrical geometry and includes electrostatic plugging of the cusping magnetic fields. The ion source is electron bombardment ionization of a controlled leak of thermal molecular hydrogen directly inside the trap, and a potential well created by those selfsame electrons is the mechanism of ion confinement. The ion trap is unique in that the confinement volume has relatively minimal external static electric and magnetic field intrusion into the regions intended to confine ions, and no overall axial magnetic field. Another standout feature is the inclusion of electrostatic elements in two locations inaccessible to electrons inside the trap that provide axial ion confinement in conjunction with electrons in the trap. Build-up of ions, and therefore confinement, was demonstrated via an ion signal that increased in intensity over a period of several dozen expected axial ion transit times while injecting electrons. A study has been conducted for a range of incident electron currents from the electron flood gun for several fixed partial pressures of molecular hydrogen and interpreted using a full particle-in-cell simulation of the trap. Data were acquired via a micro-channel plate and phosphor screen assembly biased in a manner that could only be excited by positively charged particles exiting the trap. An order of magnitude estimate for mean lifetime is made using a combination of simulated charged particle population estimates and measured data.

I. INTRODUCTION

Electromagnetic plasma and particle traps see a wide variety of applications, from the confinement of fusion plasmas, to studies of recombination, or storage of populations of particles such as antiparticles that cannot be allowed to interact with other populations. The use of overlapping electro- and magneto-static fields to form artificially structured boundaries (ASBs) for charged particle confinement is one design approach that has been predicted to be suitable for several trap geometries [1], [2].

A common approach to charge particle confinement is the Penning–Malmberg trap [3], [4], [5]. These typically cylindrical traps achieve radial and axial charged particle confinement by two different mechanisms. Three axially spaced concentric cylindrical electrodes, with the middle electrode grounded and the outer electrodes equally biased, are used to create a potential well suitable for axial confinement of charged particles. According to Earnshaw's theorem we know

that this electrode configuration forms an electric potential saddle, confining particles axially and accelerating them out of the trap radially. To establish radial confinement a uniform axially-aligned magnetic field is used, forcing particles that would otherwise accelerate out of the trap into gyroscopic trajectories. Penning–Malmberg traps, as detailed, are suitable for confining particles of only one sign of charge.

To study physical phenomenon like atomic recombination a trap must be able to confine charged particles of both signs in a single volume. A modification to the Penning trap design that gives it this key ability is nesting additional potential wells suitable for confining one sign of charge inside a standard Penning trap potential well suitable for confining the other sign of charge, done by way of including additional interior cylindrical electrodes. This design is termed a nested Penning trap [6], [7], [8], [9] and has been used in landmark studies such as the ALPHA [10], [11], ATRAP [12], [13], [14] and ASACUSA [15], [16] experiments.

The charged particle trap detailed in this paper is most comparable to the ALPHA-2's magnetic multipole minimal-B trap. Minimal-B traps confine charged particles in localized volumes of minimal magnetic field strength by way of field cancellation inside volumes of increasing magnetic field strength[17], [18], [19]. ALPHA establishes a minimal-B volume using a combination of mirror coils to create axial minima and an octupole to create a radial minimum. These elements are immersed inside a large uniform axial magnetic field. Coinciding with the minimal-B volume is a nested penning trap produced by a stack of cylindrical electrodes. Charged particles inside the minimal-B volume traveling out of the volume tend to be deflected back toward the minimal-B volume, forming three-dimensional (3D) magnetic mirror confinement. This magnetic field configuration is commonly termed a cusp trap. Minimal-B traps have advantages over Penning-Malmberg traps because they are capable of confining neutral particles as well as charged particles, a key advantage of radial and axial magnetic confinement [20].

In our experiment we aimed to demonstrate the principle of two-species confinement using space charge without externally generated nested potential wells. We chose the system of electrons and H_2^+ . Electrostatically our trap is configured to confine electrons, which serve the role of our mobile charge species. We lack the superconducting coils necessary to generate the multi-tesla magnetic fields commonly seen in other traps and therefore the limit on the electron energies we can confine is approximately 60 eV. Electron leakage and loss

1

due to background gas collisions were nonnegligible, so we continually supplied electrons. Technical constraints and the electron energies limited our ability to introduce sufficiently cold H_2^+ from outside of the trap, so we instead took advantage of the non-zero rate of electron impact ionization of molecular hydrogen (H_2) by 60 eV electrons to produce thermal H_2^+ inside the trap. With this system we have demonstrated the space charge confinement of H_2^+ by way of the build-up of substantial amounts of H_2^+ inside the trap when the trap was "closed" versus a relatively constant background ionization when the trap was "open". In this paper we provide data from experiments indicative of this result and present the results of corroborating Particle-In-Cell (PIC) simulations.

This paper is organized as follows. Section 2 presents the physical apparatus and the experimental methods along with the involved reasoning. Section 3 presents the preliminary simulations used for the trap's design and experimental development. These sections are presented in this order for clarity but chronologically the simulations and experiments were developed concurrently and should be considered together. Section 4 presents the results of the experiment and Section 5 provides an analysis and discussion of the results. Section 6 contains concluding remarks.

II. EXPERIMENTAL APPARATUS

A. Physical description of the apparatus

The experimental apparatus was designed to probe build-up of H_2^+ over time, after introduction of electrons into a volume designed to trap the ions produced. The components of the experimental apparatus were an electron gun, an einzel lens, a space-charge based ion "trap", a microchannel plate (MCP) and phosphor screen assembly (MCP-PS assembly), a charge-coupled device (CCD) camera, a vacuum system, a controlled gas source, and electronics for control of the experiment and acquiring data. Figure 1 shows the einzel lens, trap, and MCP-PS assembly. The electron source was an electron gun with a tungsten thermal emitter, set to produce 60 eV electrons.

The electrons from the gun were emitted directly into an axisymmetric einzel lens (elements labeled 2 and 3 in Fig. 1). The einzel lens was used to control the flow of electrons from the electron gun into the trap by varying the voltage applied to the middle element.

We utilized rare-earth permanent ring magnets in the construction of the space-charge-based ion trap to create the necessary magnetic fields. The trap is axisymmetric and consists of all elements between and including the entrance and exit beveled elements (60° opening angle; labeled 4 and 8 in Fig. 1). Table 1 lists the dimensions and Fig. 1 label for each element of the trap.

Element	I.D(mm)	Thickness(mm)	Fig. 1 Label	
Beveled electrode	12.7-20	6.35	4,8	
Gate electrode	12.7	2.03	5	
Magnets	14.05	3.125	6	
Plugging electrode	22.22	2.03	7	
Table I				

ELEMENT DIMENSIONS

The (12) axially magnetized NdFeB n42-grade magnets with a residual magnetization of 1.28 T alternate with 13 plugging electrodes. The magnets are aligned such that like magnetic poles face each other in a north-north south-south configuration. The plugging electrodes have a larger internal diameter than the magnets to limit the inward radial intrusion of the electric field. The conducting elements are electrically insulated from each other by mica disks with an average thickness of 0.45 mm located between the axial faces of adjacent elements. The mica is recessed ~1.6 mm from the inner radial surfaces to reduce or eliminate any potential capacitive charging effects. Elements 2-5 and 7-9 in Fig.1 are made of oxygen-free high-conductivity Cu. The overall length of the ion trap is 9.3 cm and the enclosed volume is ~11.8 cm³.

Charged particles were detected with the MCP-PS assembly, which consists of two microchannel plate electron multipliers (7.8 cm² active area; labeled 10 and 11 in Fig. 1) mounted in a chevron pair configuration with an attached phosphor screen (labeled 12 in Fig. 1). In operation, the intermediate microchannel plate faces were grounded, and the front face, back face, and phosphor screen were biased appropriately to produce an ion-to-electron-to-photon conversion chain, which could then be photographed by the CCD camera. The camera was positioned to have only the phosphor screen in its field of view.

The electron gun, einzel lens, ion trap, and MCP-PS assembly were mounted in a turbo-molecular-pumped ultra-high vacuum chamber with a base pressure of 5×10^{-9} Torr. During an ion trapping experiment, H_2 gas was introduced into the vacuum chamber near the ion trap by means of a controlled continual leak from a high purity ($\sim99.999\%~H_2$) gas source. Due to the low base pressure, it is expected that, while the leak was ongoing, the composition of the background gas in the vacuum chamber was approximately the same as that of the leaked gas. The H_2 leak was not shut off at any time during an experiment, because the several minute pump-out time of the H_2 gas from the chamber and trap was much longer than that of an experimental cycle.

B. Operation

The einzel lens, ion trap, and MCP-PS assembly were operated in the following three-stage experimental cycle by varying the biases on three elements while keeping other elements and components fixed. The fixed elements were the following. The plugging electrodes were biased to $-80~\rm V$ to repel electrons traveling into the magnetic ring cusps between each pair of magnets. The front face of the front MCP-PS was biased to $-1000~\rm V$ to repel any electrons and attract ions. The phosphor screen was biased to $1800~\rm V$ to attract electrons generated by ion impacts on the MCP pair for conversion into photons. The ring magnets, gate electrodes, entrance beveled element, outer einzel lens elements, and shielding electrode were grounded. The electron gun was always on. The camera initiated the three-stage cycle at the beginning of an image exposure and collected light for all three stages.

The middle einzel lens was set to one of two different voltages, -74 V and -44 V, and was used to control electron

flow through the lens assembly. Electrons were able to pass through the lens when the voltage was at -44 V and the lens was considered "open". Electrons were unable to pass through the lens when the voltage was at -74 V and the lens was considered "closed".

The exit beveled element was set to either 0 V or -130 V, and was used to control electrons leaving the trap through the trap's rear. Electrons were able to exit the trap when the voltage was at 0 V, corresponding to the exit being "open". Electrons were unable to exit the trap when the voltage was at -130 V, corresponding to the exit being "closed".

The back face of the MCP chevron pair was set to either 0 V or 1000 V, and was used to control the MCP-PS assembly's ability to emit light, and therefore detect ions. When the potential was at 1000 V the MCP-PS assembly was considered "on", i.e., able to convert detected ions into light. While the potential was at 0 V the back MCP prevented the conversion of ions into light, so the MCP-PS assembly was considered "off".

Time-dependent operation of the einzel lens, ion trap, and MCP-PS assembly was established by varying the biases on three elements (labeled 3, 8, and 11 in Fig.1) to create a cycle with three stages (Fig. 2). During the "empty" stage, there was no electron injection into the trap (black circles in Fig. 2). During the "loading" stage, electrons were injected into the trap and ion accumulation occurred (open triangles in Fig. 2). During the "unloading" stage, electrons continued to be injected into the trap, but ion release toward the MCP also occurred (black diamonds in Fig. 2). The three-stage cycle is different from the operational cycle of a Penning trap that includes a holding stage immediately after a loading stage. Instead, loading and holding of ions occurred simultaneously, because ion loading (by electron bombardment ionization of continually supplied H₂) and ion confinement (using electron space charge) both involved the presence of continually resupplied electrons. It was necessary to continually resupply the electrons, because the electron lifetimes in the trap were short (at most a few microseconds) compared to the times of interest in the study.

The voltages applied to elements with variable biases during a portion of the empty stage, all of the loading stage, and a portion of the unloading stage for a representative cycle are plotted in Fig. 3. During the empty stage, the einzel lens and exit beveled element were closed to the passage of electrons, and the MCP-PS assembly was off. The trap transitioned from the empty stage to the loading stage at the start of a pulse (at time $t = 20 \mu s$) shown in Fig. 3(a). The transition occurred when the voltage on the middle einzel electrode was switched from -74 V to -44 V, thereby opening the einzel lens to allow electrons to pass from the electron gun into the trap during the loading stage. Also during the loading stage, the exit beveled element remained closed to passing electrons, and the MCP-PS assembly was off. The duration of the loading stage varied during experimentation from 5 μ s (Fig. 3(d)) to 1550 μ s to allow for probing of H₂⁺ build-up over time.

The unloading stage started when the exit beveled element's bias was raised from -130 V to 0 V, thereby opening the exit beveled element to the passage of electrons. As described

in the next section, the associated change to the electron space charge caused trapped ions also to pass through the exit beveled element. The bias on the back MCP was raised from 0 V to 1000V, turning the MCP-PS assembly on, which began the detection of ions. Though an image was being acquired during all three stages the only visible light emitted by the phosphor screen was while the MCP-PS assembly was on during the unloading stage. The pulse turning the MCP-PS assembly on was always 100 μ s long so any data collected via an exposure associated with ion detection was during this 100 μ s window. A cycle concluded with the end of the camera exposure and the trap returned to the empty stage.

Figure 4 presents a typical magnetostatic (Fig. 4(a)) and electrostatic (Fig. 4(b)) field configuration for the applied voltages detailed in Fig. 3 during the loading stage of operation (Fig 2). The magnetostatic fields were calculated with RADIA [21] and electrostatic fields were calculated using XOOPIC [22]. Much like a Penning trap, axial confinement for electrons that travel along the axis of symmetry is provided by an electric field. Unlike a Penning trap, radial electron confinement is not provided by a uniform axial magnetic field. Instead, radial confinement of electrons is provided by a combination of a magnetic field that forms ring cusps between each pair of magnets and an electric field that reflects electrons that enter the cusps. Also, axial electron confinement away from the axis of symmetry is provided by a magnetic field that forms point cusps at each axial end of the trap's interior.

Image exposure time was 120 ms. One image was acquired per experimental cycle. Image data were integrated across the entire 100 μ s interval the MCP-PS was on (Fig. 3(c)), and the remainder of the 120 ms camera image exposure was dark. A total of 12 sets of data were acquired. Data were collected at three pressures with two electron beam currents for two distinct experiments per beam current. In one experiment there was no loading stage (the beveled exit element was left at 0 V for a direct transition from empty to unloading) and in the other there was a loading stage. All timings and voltages were otherwise identical between the two trials for each pressure. Direct comparison between these two trials provided a measure of what portion of H₂⁺ was building up (with a loading stage), as compared to a steady-state signal where any ions created could immediately be lost (without a loading stage). At each pressure and electron beam current a minimum of 1600 exposures were taken for each trial. Each set of 1600 (or more) images was divided between 31 different build-up times and a dark control, to give at least 50 exposures for each build-up time. Each set of 32 images was taken sequentially with a 1 second delay time between each loading cycle. The variation of the build-up time was controlled by a micro controller running a simple c program. Starting at 5 μ s, the loading time was increased by 50 μ s for each successive exposure in a sequence. The 32nd cycle was used as a dark control exposure to subtract out a signal from the MCP-PS assembly caused by ultraviolet light from the electron gun, a signal with an identical contribution (within the camera's noise floor) to any image with the same beam current and MCP excitation time and independent of background pressure. The control images were taken with the trap left in the loading stage.

III. SIMULATIONS

The trap was initially designed in full using the particle-in-cell (PIC) program XOOPIC [22]. XOOPIC simulates dynamic space charge phenomena and charged particle motion, and comes paired with a Monte Carlo collisional model to simulate plasma interactions with neutral background gas. Presented here in Sec. III is a simulation of the accumulation of ionized hydrogen within the space charge distribution of a continuously resupplied electron cloud.

A number of simulated time spans of trap operation are presented below. The simulations were used to study the early evolution of the trap immediately after introduction of electrons. Technical constraints imposed by hardware resources and computation time limited the total span of simulated time possible, so simulated equilibrium was never reached. To compensate for this the authors instead chose to study specific operational cases of the trap and to use the simulated results to inform a rate equation model discussed in section 5. The motivation for the simulations was to aid in description of our experimental results, which were a direct measure of the time taken to reach total system equilibrium. The longest simulation time span was 300 μ s.

The simulated environment was a two-dimensional grid adapted to a cylindrically symmetric geometry containing all trap elements shown in Fig. 1, inclusive of and between the entrance beveled element and the shielding electrode. The grid had 1008 grid spaces axially and 128 grid spaces radially, with adjacent grid points 0.15625 mm apart axially and 0.125 mm apart radially, for a total spatial grid size of 157.5 mm by 16 mm. XOOPIC allows for subdividing grids to define boundaries that would otherwise not fall on grid points, and each included element's placement and physical dimensions matched Fig. 1 to within \sim .1 mm. All conductive elements were defined with the Dirichlet boundary condition with voltages matching those in Fig. 1. All simulations were conducted with time steps of 5×10^{-13} s.

The cylindrical axis of rotation ($-62.5 \text{ mm} \le z \le 95 \text{ mm}$, r = 0), radial outer boundary ($-62.5 \text{ mm} \le z \le 95 \text{ mm}$, r = 16 mm), front cylindrical cap (z = -62.5 mm, $0 \le r \le 16$ mm), and rear cylindrical cap (z = 95 mm, $0 \le r \le 16$ mm) were all defined with Neumann boundary conditions except where those boundaries coincided with conductive elements, which used Dirichlet boundary conditions. Any particle that crossed the cylindrical axis along (r = 0) was mirrored back into the simulated environment which is typical of two dimensional formulations of axially symmetric 3D cylindrical systems, and any particle that reached any other boundary was removed from the simulation. An electron beam was defined at (z =-62.5 mm, $0 \le r \le 2$ mm) with an initial kinetic energy of 60 eV per electron near the center of the rightmost grounded einzel lens electrode (labeled 2 in Fig. 1). A monoenergetic beam was chosen as the electron source for the simulation, because the specifications for the electron flood gun used in the experiment indicated a total kinetic energy variation of $\pm 1\%$. The electrons in the beam had randomized initial positions on a 4-mm-diameter axisymmetric disk. The kinetic energy of each electron was distributed between cylindrical velocity components by defining $V_r = \rho \sin(\varphi)$ and $V_z = \rho \cos(\varphi)$ and randomly sampling an inclination angle $0 \le \varphi \le 20^\circ$ from the cylindrical axis z for $\rho = 4.5941 \times 10^6$ m/s (corresponding to a 60 eV electron). The beam current was set to .5 μ A. Fundamental to PIC codes is the real-to-virtual particle ratio, a simplification that treats single virtual particles as though each particle has the mass and charge of many particles. The real-to-virtual particle ratio was 200:1 for electrons, ions and gas particles, but numerical values are reported after being converted back to real particles, unless noted otherwise.

The simulation included only three species of particles. The species were primary electrons emitted by the electron gun, ionized hydrogen created by the electron impact ionization of the background hydrogen gas, and the resultant secondary electrons from the ionization event. Background hydrogen gas was treated as a local particle density specific to a given location and not tracked individually. The only direct particle interactions included in the simulation were primary electron impact ionization of background hydrogen gas. Fundamental to XOOPIC, inter-species interactions are described through the space charge interaction. Not included in the simulation and unavailable in XOOPIC were secondary electron collisional interactions with ions or neutral background gas, and ion collisional interactions with neutral background gas. These unincorporated phenomena are expected to occur at 3-5 orders of magnitude lower rates than the included interactions due to low particle density and background pressures. The phenomena not included are discussed in more detail in Section 5.

In the simulation atomic hydrogen gas was uniformly distributed in the simulated trap with a number density of 5.52×10^{16} m⁻³ as a model of a neutral background gas. The hydrogen gas was monoenergetic and defined to have a temperature of 293 K (\sim 0.025 eV). H₂ is unavailable in XOOPIC, so the simulated gas was selected to be atomic hydrogen (H) with modifications to compensate for differences in ionization cross sections between the two species. For 60 eV electrons such as those introduced into the trap, the total impact ionization cross section for H_2 (1.015 A^2) is larger than for H (0.612 A^2 [23]) so if uncorrected XOOPIC was expected to underestimate ionization rates. As a first-order correction to the cross section of H, the pressure, and therefore neutral density, was increased by the ratio of H to H₂ ionization cross sections, i.e., from 1×10^{-6} to 1.659×10^{-6} Torr, to estimate ionization behavior for H_2 at 1×10^{-6} Torr. The particle definition of H used by XOOPIC was modified to use the mass of H_2 .

XOOPIC uses a Monte Carlo implementation [24] of a collisional model of electron-neutral interactions that includes both direct electron impact and tunneling ionization paths for ion creation. At each simulated time step ionization events were randomly allocated to primary electrons weighted by the probability $P=1-\exp[-n\,\sigma\,v\,\delta]$ of the event occurring. In the equation n is the number density of neutrals, σ the cross section of the impact, v the speed of the electrons, and δ the time step. The ionization rate in the trap was dictated by this calculated probability. This equation was used to justify

scaling the background neutral H pressure to simulate H_2 ($n \sigma = 5.52 \times 10^{16} \text{ m}^{-3} \bullet 0.612 \text{ Å}^2 \approx 3.29 \times 10^{16} \text{m}^{-3} \bullet 1.015 \text{ Å}^2$). A potential mechanism of interest, recombination, between H⁺ and electrons is unavailable in XOOPIC. Recombination is discussed in more detail in Section 5 of this article.

The magnetic fields used in the simulation were calculated at each grid point by RADIA and imported to XOOPIC. RADIA uses an analytical solution for the magnetic field of a magnetized polyhedron to approximate field configurations of more complex geometries [21]. The magnetic field calculated by RADIA is continuously defined. XOOPIC interpolates the magnetic field values from grid points to the location of each particle.

In the simulation spanning $300~\mu s$ electrons were introduced by the electron beam into the trap at a rate of $3.12 \times 10^6~\mu s^{-1}$ (i.e., $0.5~\mu A$). Figure 5 shows the evolution of the primary electron population over the total $300~\mu s$ duration of the simulation. Throughout the $300~\mu s$ simulation the trap was in the loading stage of operation. At the end of the simulation, the rate of loss of primary electrons from the trap was 99.2% of the rate of introduction of primary electrons into the trap. 90% of the electrons lost left the trap back through the entrance.

Simulated contours of electric potential are plotted in Fig. 6 at the ends of loading and unloading stages both with and without particles present. Unless noted otherwise, results presented in this section for loading stage simulations with particles present are from the same simulation as for Fig. 5, but for shorter durations. At 32 μ s of simulated loading time Fig. 6(c) shows the formation of multiple electric potential wells produced by the electron space charge. For example, a 3D potential energy well for ions exists between z = -3mm and $z = \sim 14.5$ mm in Fig. 6(c). In this well there are 2 virtual ions confined, corresponding to 400 real ions. A 3D electrostatic potential well cannot occur in vacuum according to Earnshaw's theorem. Here the 3D wells in a volume relatively free of externally produced fields are established by the dynamic equilibrium (or quasi-equilibrium) of the electron cloud. Figure 7 displays the positions of virtual electrons, and of virtual hydrogen ions that remain energetically trapped, at 32 μ s. We define trapped ions here as having a kinetic energy less than the difference in potential energy between the ion's location and the position on the edge of the confining well with the lowest potential, a point that is always on the z axis.

In Fig. 8, multiple axial potential wells are clearly visible, for this and other loading times. To explore the effect of the trap state on ion confinement, three comparative simulations were run (Fig. 9). Each began with a 63 μ s loading stage, followed by a 43 μ s second stage to simulate (1) a continuation of the first loading stage; (2) a holding stage with the trap set for loading but without background H gas present; and (3) an unloading stage without background H gas present to see if and how H ions leave the trap while unloading. At 63 μ s there were total of 9200 ions trapped in the various potential wells and an additional 7000 ions with energies within 5% of being confined.

At the conclusion of the 43 μs second stage of continued loading, with background H present and a -130 V bias on the exit beveled element, there were 26,200 trapped ions and

an additional 14,400 ions with energies within 5% of being confined.

At the conclusion of the 43 μ s holding second stage without background H present and with a -130 V bias on the exit beveled element, 200 ions had been lost from the 9200 ions that were energetically trapped at 63 μ s. The rate of ion loss had decayed substantially by simulation's end.

At the conclusion of the 43 μ s second unloading stage without background H present and with no bias on the exit beveled element, 1600 ions had been lost from initial trapped ion population of 9200 at 63 μ s, and 4000 ions had been lost from the 7000 ions with energies within 5% of being energetically confined at 63 μ s. This simulation can be used to estimate what populations of ions would reach the MCP-PS assembly were one to attempt a measurement. During the 43 μ s of the second stage, 2200 ions reached the simulation boundary at z = 95 mm with trajectories that would be expected to reach the MCP-PS assembly in the physical experiment. Of the 2200 ions that reached the simulation boundary, 800 ions were from the trapped ion population of 9200 at 63 μ s, and the remaining 1400 ions were from the 7000 ions with energies within 5% of being energetically confined at 63 μ s. The remainder of lost trapped ions (800 ions) had not yet reached the simulation boundary but had trajectory towards the MCP-PS assembly. Of the remaining 7600 ions still trapped, effectively none would reach the MCP-PS assembly as all of these ions had substantially higher radial velocities than axial velocities. All trapped ions with trajectories towards the MCP-PS were located in the well located between (3 mm \leq z < 14 mm). From the total ion population of 191,200 at 63 μ s, 33200 had trajectories that would reach the simulation boundary eventually. Uniformly, unconfined ions had larger r velocity components and tended to be caught by the electrodes intended to deflect electrons unless they were formed near the exit of the trap.

Figure 8 shows that the potential wells in which ions were confined changed over time as more electrons were added to the trap. For example, the points of highest and lowest electric potential along the z axis at 32 μ s for the well located approximately at (-10 mm \leq z \leq 3 mm) changed from -0.230 V and -0.281 V, respectively, to -0.280 V and -0.352 V at 63 μ s. The corresponding points of highest and lowest potential at 106 μ s for the same well changed to -0.305 V and -0.401 V, respectively (not shown). The difference in potential increased from 0.051 V at 32 μ s to 0.072 V at 63 μ s to 0.096 V at 106 μ s. In the extended 300 μ s simulation the dynamic evolution of the potential wells continued for the duration, leading to the conclusion that the trap had yet to reach equilibrium. Longer simulation times were not possible due to technical constraints.

IV. EXPERIMENTAL RESULTS

To obtain signal from ions exiting the trap, a region of interest (ROI) was established in each image from the CCD camera. The ROI was identical across all trials: the same 30x30 pixel square centered on the beam spot in each image. Figure 10 shows examples of typical ROI images. The camera images reported pixel values in analog-digital units (ADU). To

estimate a number of ions associated with a given mean ADU value for the pixels in an ROI we present a conversion formula built from the conversion factors of each stage of ion detection, $1 ion \cdot a^2 \cdot b \cdot c \cdot d \cdot e \cdot f \cdot g^2 \cdot h^{12} \cdot i \cdot 1/j$. The parameters were obtained from manufacturer specifications, common estimates for light transmission through various surfaces, and published data. The various factors are a = .95 for two 95% transmission wire grids in front of the microchannel plate assembly, b = .52 electrons/ion for the detection efficiency [25] of the MCP plate pair for H_2^+ ions, $c = 5 \times 10^6$ electron gain (from manufacturer's specifications) for the MCP pair at 2kV bias, d = 8×10^{-4} photons/electron associated with an estimated .08% [26] quantum efficiency of the p20 phosphor, e = .79 for the 79% transmission of the fiber optic plate [27] on which the phosphor was deposited, $f = 5.4 \times 10^{-3}$ for the weighted fractional solid angle subtended by the 52mm lens located 25 cm behind the phosphor screen, g = .96 for 4% light lost from each surface of one window, h = .99 for 1% light lost from each surface of 6 coated glass elements in the camera lens, $i = .66 \, \frac{electrons}{photon}$ for the quantum efficiency of the image sensor (manufacturer's specifications) at the phosphor's peak wavelength (560 nm), and $j = 2.68 \frac{electrons}{ADU}$ for the conversion gain for camera. The final conversion was 1 ion = 1.62 ADU by the MCP-PS assembly and camera.

Presented in Fig. 11 are the experimental data for ions detected by the MCP-PS assembly. Each plot shows results for equal length trials both with and without a loading stage. The measurements from trials with a loading stage exhibited bounded growth of signal associated with ions over loading intervals of 5 μ s to 1555 μ s. In contrast, trials without a loading stage did not vary significantly in intensity over time. The plots are labeled with both the electron current falling on interior surfaces of the trap and the background pressure during each experiment. The pressures selected were 1×10^{-6} (Fig. 10a, 10b), 5×10^{-7} (Fig. 10c, 10d), and 6×10^{-8} (Fig. 10e, 10f) Torr. The results indicate that the total number of ions measured was greater when a loading stage was used. Note that for the 6×10^{-8} Torr trials the ionization rate was much lower than for other pressures. Also note that the ion signal from the trap at 6×10^{-8} Torr was clearly not close to saturation as its growth still appeared to be linear over the measured interval.

To demonstrate the effectiveness of the radial ASB, Table 2 lists the steady-state electron current falling onto interior surfaces of the trap with and without electrostatic plugging of the magnetic ring cusps. These current measurements were found to change by less than 0.5% when the bias on the exit beveled element varied from 0 V to -130 V.

Torr	Plugged (nA)	Unplugged (nA)	
1×10 ⁻⁶	-104	-282	
	-120	-317	
5×10 ⁻⁷	-105	-280	
	-124	-325	
6×10 ⁻⁸	-105	-272	
	-119	-319	
Table II			

CURRENT REACHING INTERIOR SURFACES OF ELECTRODES BOTH WITH A BIAS ON THE PLUGGING ELECTRODES (PLUGGED) AND WITHOUT A BIAS (UNPLUGGED).

V. ANALYSIS AND DISCUSSION

Some key differences between our trap and the ALPHA-2 trap are that we do not use a large uniform axial magnetic field, we do not use an octupole/multipole to establish radial magnetic confinement, and we are not using superconducting magnets. We use a "linear array of magnetic field ring cusps" [28] to establish multiple minimal-B volumes inside the trap to form a magnetic trapping volume similar to a multicusp trap [29], [30]. These ring cusps are formed using axially-magnetized rare-earth permanent ring magnets aligned axially with magnetic poles in a north-north south-south configuration. This configuration produces 3D magnetic near-nulls between each pair of magnets.

Our design allows three primary advantages over single cusp minimal-B, nested Penning, and other multi-cusp traps. First, using permanent magnets allows us to avoid using prohibitively expensive superconducting anti-Helmholtz coils and allows us to produce strong minimal-B confinement volumes more compactly. Second, we are able to use electrostatic fields to reinforce the cusping magnetic field confinement both axially and radially while maintaining minimal electric field intrusion into the trapping volume. In our trap the fields used to confine charged particles are primarily situated around the edge of the confinement volume as ASBs and the actual confinement volume is relatively free of external fields. Third, we do not need to nest additional electric potential wells with external electrodes to confine particles of both signs of charge. In agreement with Pacheco et al.[1], [31] our simulations predict that in a confined volume with minimal external field intrusion a more populous low mass charge species will form a 3D electric potential well suitable for confining a higher mass, lower energy species of opposite charge through a dynamic interaction between the two species and the space charge of the lower mass species. This allows for an effective electrostatic confinement of the higher mass charge particle species and circumvents Earnshaw's theorem. [31], [32], [33] A typical nested Penning trap, by establishing nested potential wells with external fields, segregates the trapping volumes of the two signs of charge which inhibits mixing of the two species. In our trap the nested potential well itself is established by one species for the other and the two volumes inherently overlap.

Ion confinement in a cylindrical volume can be broken up into radial and axial parts (although the two may be coupled). Functionally, the trap's performance has been tested in a configuration where radial ion confinement was always maintained and axial ion confinement was established and then relaxed. The potentials used to plug the magnetic field cusps and reflect electrons back into the trap radially are deeply attractive to ions. An additional numerical trajectory simulation of the trap using SIMION [34] with the trap biased to the unloading configuration and without electrons was conducted. For thermal ions with random trajectories and random starting locations in the range ($-37.5 \text{ mm} \le z \le$ 37.5 mm, r < 16 mm) fewer than 0.1% of ions reached the MCP-PS assembly. Ions reaching the MCP-PS assembly in the simulation all had initial positions $z \ge 35$ mm. Thus, that we observed a strong ion signal at the MCP-PS assembly indicates radial ion confinement that does not fully dissipate while electrons are present and the trap is open. We can conclude that axial ion confinement was established by electron space charge with two pieces of evidence. First, there was no signal from the MCP-PS assembly while the exit beveled element was biased to -130V while electrons were flooding the trap. Second, the ion signal grew in intensity in experiments with a loading stage and remained relatively constant for experiments without a loading stage.

To assist in interpreting our results, a linearized system of phenomenological rate equations describing particle populations in the trap was developed and solved numerically to reproduce simulated results, as shown in Fig. 12(a). The rate coefficients were fit to simulated data of charged particle population growth in the well located at (3 mm \leq z \leq 14 mm) in the 300 μs simulation described in Section 3 (background pressure 1×10^{-6} Torr and a -500 nA electron beam). Fig. 12(b) compares the measured ion data from the experimental trial at 1×10^{-6} Torr and -120 nA (a reminder: this is not the total electron beam current, but the current falling on measurable surfaces) to the simulated trapped ion build-up from the 300 μs simulation and the rate equation solution for the trapped ion population. The time scales for both the simulated and measured data are in good agreement and we argue that the two systems are closely related. The rate equations are

$$\frac{dN_p}{dt_s} = R_p - \alpha N_p - \beta N_s + \gamma N_u
\frac{dN_s}{dt} = \delta N_p - \epsilon N_s
\frac{dN_u}{dt} = \delta N_p + \rho N_s - \zeta N_u
\frac{dN_i}{dt} = \omega \left(N_p - \xi N_u + \psi N_s \right) - \chi N_i.$$
(1)

In this system of equations N_p represents the population of primary electrons, N_s the population secondary electrons, N_u the population of unconfined ions in the trapping volume, and N_i the population of confined ions. Among the terms on the right of (1) are the sources and sinks assumed to arise from relations of the form $\frac{dN}{dt}=V\,n_1\,n_2<\sigma\,v>$, where N is the population of the resultant, n_1 and n_2 are the two reactant densities, assumed to be approximately spatially uniform within volume V, and $<\sigma v>$ is the product of reaction cross section σ and relative speed v, averaged over the velocity distribution. If one of the reactant densities n_1 , such as for the neutral gas, is approximately constant, then the rate coefficient becomes $n_1 < \sigma v >$. The rate constant and coefficients associated with the primary electron population change $\frac{dN_p}{dt}$ are R_p (fit value = 1.82×10^{11}) for the constant rate of primary electron introduction into the trapping volume from the electron gun; coefficient α (= 3.01×10⁵) for loss of primary electrons exiting the trap; β (= 2.04×10⁵) for loss of primary electrons due to the repulsive space charge from secondary electrons in the well; and γ (= 1.98×10⁶) for the effective enhancement of primary electron admittance due to the attractive space charge from ions in the well. Parameters β and γ are used to describe volumetrically averaged phenomena, i.e., collective space charge interactions between species. Similar parameters are used for all interactions coupled through space charge in the rate equation system. The rate coefficients associated with the secondary electron population change $\frac{dN_s}{dt}$ are δ (=

1560) for ionization events inside the well and ϵ (= 440) for secondary electrons lost from the well offset by those entering from outside the well (as a collective loss term). Rate coefficients associated with the free ion population change $\frac{dN_u}{dt}$ are δ (= 1560) for ionization events inside the well, ignoring the small correction for those creating trapped ions; ρ (= 1450) for the reduction to the rate of loss of free ions due to the attractive space charge of secondary electrons; and ζ (= 1.37×10^4) for the loss rate of free ions, including a component due to repulsion by the ions' own space space charge. Rate coefficients associated with the trapped ion population change $\frac{dN_i}{dt}$ are ω (= 175) for the trapped ion production rate and space charge well depth associated with primary electrons; ξ (= 9.05) to describe how effective the more numerous free ions are at neutralizing the space charge well which confines the trapped ions and thereby modifying the production rate; ψ (= 0.97) for the effective enhancement of the space charge well by secondary electrons; and χ (= 1100) for the loss rate of trapped ions. Not included in this simplified linear model is a term that encompasses the $\sim 25 \,\mu s$ delay in the onset of trapped ion formation due to lack of an appreciable space charge well in which to hold them before that time (Fig. 8). We introduce a time shift in Fig. 12(b and c) to compensate for this. Other terms in the rate equations, such as for the trapped ions' contribution to primary electron admittance, were negligibly small and were omitted for simplicity.

In this model we neglect recombination of the trapped ion populations (either H⁺ or H₂⁺) as a potential loss mechanism for trapped ions for both practical and physical reasons. First, XOOPIC has no mechanism for recombination so our simulated ion data do not have a contribution from that phenomenon. Additionally, our experimental apparatus was incapable of detecting the recombined neutral particles. We feel this neglect of recombination is justifiable for the following reasons. First, in the ion confinement well considered in the model above, the averaged trapped ion density is ~ 10 $\frac{Ions}{mm^3}$ and with a roughly thermal mean kinetic energy. To recombine, ions require an overlapping population of electrons cool enough for capture (radiative/three-body). Neglecting the nearly monoenergetic and relatively hot 60 eV primary electrons, the only available electron population comes from the secondary electron population. The mean kinetic energy of secondary electrons while crossing the well was \sim 7 eV. Assuming every secondary electron (5.5×10^4) in the volume occupied by trapped ions and every trapped ion (1.6×10^4) in the well was involved the product of $\sigma_r N_s N_i v_s$ yields an estimated instantaneous rate of \sim 1 to 13 recombined ions per second using the range of recombination cross sections $\sigma_r \approx$ 0.1 to 1 \mathring{A}^2 found in literature for thermal H_2^+ [35], [36], [37], [38] and electrons with a mean speed (v_s) of $\sim 1.4 \times 10^6$ m/s. Through extrapolation of final populations using N_s and N_i the equilibrium recombination rate was ~ 14 to 145 recombined ions per second. This rendered recombination a negligibly small missing component of our model, at least in the time range we were able to study. This estimated recombination rate for trapped ions is likely a gross overestimate for the actual recombination rate in our trap. The source of our secondary electron population is all ionization events inside trap and potential partners for recombination were every ion in the well. There were 2×10^5 untrapped simulated ions in the well at 300 μ s. The higher negative electric potential around the well leads to a lower kinetic energy and more likely capture for secondary electrons by the still relatively cool and more numerous untrapped ions (mean kinetic energy of 0.12 eV).

The model system of rate equations helps to understand the driving mechanisms occurring in a single well within the trap but does not capture all the physics as an entirely linear model. The parameter χ (treated as a exponential decay constant) with the trap closed and with background H gas present leads to an estimated mean ion life time of $\sim 900 \ \mu s$. This loss rate does not hold true when the background H gas is turned off in simulation. The total ion population in the simulation of trapping and holding ions without background H approached an asymptote of 7600 ions, all of which are assumed to be trapped ions. The primary (and arguably only) mechanism for trapped ion loss available in XOOPIC is due to the introduction of additional ions. The trapped ion population, while small in comparison to the total ion population, resides in a small spatial volume and within a shallow potential well. As additional ions are introduced the confining electron space charge is neutralized, decreasing the depth of the confining potential well and causing evaporation from the trapped ion population. Important phenomena not included in XOOPIC are recombination, ion-ion collisions, electron-ion collisions, and ion collisions with background neutrals. Only the last two processes and recombination are expected to be efficient enough to be relevant in our studied time range but with effects too small to resolve in our data. The background gas in actual experiments was roughly 99% H₂ at 1×10⁻⁶ Torr for the highest-pressure trials, so the collisional frequency of ions with neutrals under some simplifying assumptions (ions and background gas treated as having the same kinetic radius) was \sim 19 <u>collisions</u>. Again under some simplifying assumptions (H₂⁺ being static in comparison to electrons, and only 20% of 60 eV electrons passing through the trapping volume), an upper limit for the coulombic collisional rate between 60 eV electrons and ions in the trapping volume was $\sim 10 \frac{collisions}{collisions}$, integrated across all scattering angles imparting enough energy to free an ion (scattering cross section <1 A^2). From the simulations and our rate equation model we conclude that the primary source of trapped ion loss is the introduction of addition ions. This leads to the conclusion that trapped ion lifetime is primarily limited by pressure in the chamber. This analysis (and the rate equation fits) cannot be applied directly to our experimental data without the use of simulated data. The measured data we recorded are an inseparable convolution of fully trapped, loosely confined, and free ions near the exit of the trap while unloading.

To get an order of magnitude estimate of a mean trapped ion lifetime from one of our experimental trials we considered the data for 6×10^{-8} Torr at -120 nA. We chose this trial under the assumption that any non-linearity associated with pressure not captured in our rate equation model should be weakest for trials at this pressure. To match our simulation to this measurement we scaled all rate constants except ω , R_n ,

and α by $\frac{1}{16.7} \approx \frac{1 \times 10^{-6}}{6 \times 10^{-8}}$ and assumed the same R_p and α as from our model. In Fig. 12(c) it can be seen that for a value of $\omega=2$ for the trapped ion production rate constant the model matches the slope of our experimental data. We then varied the trapped ion loss rate constant (χ) to probe its impact on the slope of our model's predicted curve. We found that for values of $\chi\approx40$ to 100 the slope of the model remained similar to that of our data. Above this range the curve gained concavity not apparent in the data and below this range the ion population grew too quickly. This leads to an estimated mean ion lifetime of 10 to 25 ms.

VI. CONCLUSION

In this article we have presented results from novel ion trapping apparatus that takes advantage of the space charge of a loosely confined electron cloud. The trap utilizes the concept of ASBs to produce edge confinement for electrons in an otherwise low field volume. To overcome our inability to measure certain parameters we leveraged PIC simulations with initial conditions comparable to those for our trap to aid in exploring the physics occurring inside. We found the simulation to be in good agreement with the measurements we took. We also have presented a rate equation model informed by both simulated and experimental data to aid in predicting long term evolution of the system.

For a proof of concept of space-charge-based ion confinement, the trap is a resounding success. Although experimental constraints, e.g., being unable to decouple ion supply from the confinement mechanism, made it technically unfeasible to conduct direct measurements of the ion lifetimes, the comparison of matching experiments with and without a loading stage revealed some aspects of the trapping behavior. The inclusion of radial electrostatic plugging with no overall axial or radial magnetization and supporting physical measurements differentiate this system from other comparable systems and studies readily found in the literature oriented towards ion confinement. Our hybrid simulation/rate equation analysis yielded an estimated mean trapped ion lifetime on the order of 900 μ s at 1×10^{-6} Torr and 10 to 25 ms (with the ambiguity of a specific parameter) at 6×10^{-8} Torr. These lifetimes are respectable and point to the promise of the concept. In a system which could overcome our experimental limitations, the primary driver of trapped ion loss in our results associated with the introduction of additional ions would cease to occur.

VII. ACKNOWLEDGMENTS

This material is based upon work supported by the National Science Foundation under Grant No. PHY-1803047 and by the Department of Energy under Grant No. DE-FG02-06ER54883.

REFERENCES

- [1] J. L. Pacheco, C. A. Ordonez, and D. L. Weathers, "Artificially Structured Boundary for a high purity ion trap or ion source," *Nuclear Instruments and Methods in Physics Research Section B: Beam Interactions with Materials and Atoms*, vol. 332, pp. 312–316, aug 2014.
- [2] —, "Plasma interaction with a static spatially periodic electromagnetic field," *IEEE Transactions on Plasma Science*, vol. 39, no. 11, pp. 2424– 2425, nov 2011.

- [3] D. H. E. Dubin and T. M. O'Neil, "Trapped nonneutral plasmas, liquids, and crystals (the thermal equilibrium states)," *Reviews of Modern Physics*, vol. 71, no. 1, pp. 87–172, jan 1999.
- [4] J. Danielson, D. Dubin, R. Greaves, and C. Surko, "Plasma and trap-based techniques for science with positrons," *Reviews of Modern Physics*, vol. 87, no. 1, pp. 247–306, mar 2015.
- [5] J. H. Malmberg and J. S. deGrassie, "Properties of nonneutral plasma," Physical Review Letters, vol. 35, no. 9, pp. 577–580, sep 1975.
- [6] C. A. Ordonez and D. L. Weathers, "Two-species mixing in a nested penning trap for antihydrogen trapping," *Physics of Plasmas*, vol. 15, no. 8, p. 083504, aug 2008.
- [7] E. Tardiff, X. Fan, G. Gabrielse, D. Grzonka, C. Hamley, E. Hessels, N. Jones, G. Khatri, W. Kolthammer, D. M. Zambrano, C. Meisenhelder, T. Morrison, E. Nottet, E. Novitski, and C. Storry, "Two-symmetry penning-ioffe trap for antihydrogen cooling and spectroscopy," Nuclear Instruments and Methods in Physics Research Section A: Accelerators, Spectrometers, Detectors and Associated Equipment, vol. 977, p. 164279, oct 2020.
- [8] D. S. Hall and G. Gabrielse, "Electron cooling of protons in a nested penning trap," *Physical Review Letters*, vol. 77, no. 10, pp. 1962–1965, sep 1996.
- [9] C. Ordonez, "Time-dependent nested-well plasma trap," *IEEE Transactions on Plasma Science*, vol. 24, no. 6, pp. 1378–1382, 1996.
- [10] M. Ahmadi, B. X. R. Alves, C. J. Baker, W. Bertsche, E. Butler, A. Capra, C. Carruth, C. L. Cesar, M. Charlton, S. Cohen, R. Collister, S. Eriksson, A. Evans, N. Evetts, J. Fajans, T. Friesen, M. C. Fujiwara, D. R. Gill, A. Gutierrez, J. S. Hangst, W. N. Hardy, M. E. Hayden, C. A. Isaac, A. Ishida, M. A. Johnson, S. A. Jones, S. Jonsell, L. Kurchaninov, N. Madsen, M. Mathers, D. Maxwell, J. T. K. McKenna, S. Menary, J. M. Michan, T. Momose, J. J. Munich, P. Nolan, K. Olchanski, A. Olin, P. Pusa, C. Ø. Rasmussen, F. Robicheaux, R. L. Sacramento, M. Sameed, E. Sarid, D. M. Silveira, S. Stracka, G. Stutter, C. So, T. D. Tharp, J. E. Thompson, R. I. Thompson, D. P. van der Werf, and J. S. Wurtele, "Antihydrogen accumulation for fundamental symmetry tests," Nature Communications, vol. 8, no. 1, sep 2017.
- [11] M. Ahmadi, B. Alves, C. Baker, W. Bertsche, A. Capra, C. Carruth, C. Cesar, M. Charlton, S. Cohen, R. Collister, S. Eriksson, A. Evans, N. Evetts, J. Fajans, T. Friesen, M. Fujiwara, D. Gill, J. Hangst, W. Hardy, and J. Wurtele, "Observation of the 1s–2p lyman-α transition in antihydrogen," *Nature*, vol. 561, p. 1, Sep. 2018.
- [12] C. H. Storry, M. Aggarwal, A. Akbari, F. Al-Rahawi, C. Amole, A. Batrachenko, A. Bebko, A. Carew, M. Chalfin, D. Comeau, G. Gabrielse, F. Garofalo, M. C. George, F. Goldenbaum, D. Grzonka, N. Guise, Y. Gura, T. Hansch, E. A. Hessels, D. Kolbe, S. Kotlhammer, I. Kuljanishvili, P. Larochelle, D. Lesage, B. Levitt, K. Lewis, B. Lishak, F. Markert, F. Nillius, W. Oelert, S. Patel, P. Popescu, M. Scheid, T. Sefzick, A. Speck, D. Swierad, J. Walz, M. Weel, J. Wrubel, and Z. Zang, "ATRAP antihydrogen experiments," physica status solidi (c), vol. 4, no. 10, pp. 3437–3442, sep 2007.
- [13] C. H. Storry, "ATRAP antihydrogen experiments and update," *Hyperfine Interactions*, vol. 172, no. 1-3, pp. 91–96, sep 2006.
- [14] M. Zieliński, D. Grzonka, W. Oelert, T. Sefzick, G. Gabrielse, J. DiSciacca, S. Ettenauer, R. Karla, K. Marable, M. Marshall, E. Tardiff, E. Hessels, C. Storry, D. Fitzakerley, M. George, M. Weel, A. MÃŒllers, and J. Walz, "Studies on antihydrogen atoms with the ATRAP experiment at CERN," *Acta Physica Polonica B Proceedings Supplement*, vol. 6, no. 4, p. 1093, 2013.
- [15] N. Kuroda, S. Ulmer, D. J. Murtagh, S. V. Gorp, Y. Nagata, M. Diermaier, S. Federmann, M. Leali, C. Malbrunot, V. Mascagna, O. Massiczek, K. Michishio, T. Mizutani, A. Mohri, H. Nagahama, M. Ohtsuka, B. Radics, S. Sakurai, C. Sauerzopf, K. Suzuki, M. Tajima, H. A. Torii, L. Venturelli, B. WÄŒnschek, J. Zmeskal, N. Zurlo, H. Higaki, Y. Kanai, E. L. Rizzini, Y. Nagashima, Y. Matsuda, E. Widmann, and Y. Yamazaki, "The ASACUSA CUSP: an antihydrogen experiment," Hyperfine Interactions, vol. 235, no. 1-3, pp. 13–20, nov 2015.
- [16] Y. Enomoto, N. Kuroda, K. Michishio, C. H. Kim, H. Higaki, Y. Nagata, Y. Kanai, H. A. Torii, M. Corradini, M. Leali, E. Lodi-Rizzini, V. Mascagna, L. Venturelli, N. Zurlo, K. Fujii, M. Ohtsuka, K. Tanaka, H. Imao, Y. Nagashima, Y. Matsuda, B. Juhász, A. Mohri, and Y. Yamazaki, "Synthesis of cold antihydrogen in a cusp trap," *Physical Review Letters*, vol. 105, no. 24, dec 2010.
- [17] D. Mascali, A. Musumarra, F. Leone, F. P. Romano, A. Galatà, S. Gammino, and C. Massimi, "PANDORA, a new facility for interdisciplinary in-plasma physics," *The European Physical Journal A*, vol. 53, no. 7, jul 2017.
- [18] A. G. Nikolaev, K. P. Savkin, E. M. Oks, A. V. Vizir, G. Y. Yushkov, A. V. Vodopyanov, I. V. Izotov, and D. A. Mansfeld, "Generation of high

- charge state metal ion beams by electron cyclotron resonance heating of vacuum arc plasma in cusp trap," *Review of Scientific Instruments*, vol. 83, no. 2, p. 02A309, feb 2012.
- [19] V. D. Dougar-Jabon, A. M. Umnov, and D. S. Diaz, "Properties of plasma in an ECR minimum-BTrap via numerical modeling," *Physica Scripta*, vol. 70, no. 1, pp. 38–42, jan 2004.
- [20] D. H. E. Dubin, "A magnetic trap for simultaneous confinement of neutral atoms and a non-neutral plasma," in AIP Conference Proceedings. AIP, 2002.
- [21] Chubar, Oleg, Elleaume, Pascal, Chavanne, and Joel, "A three-dimensional magnetostatics computer code for insertion devices," *Journal of Synchrotron Radiation*, vol. 5, no. 3, pp. 481–484, May 1998. [Online]. Available: http://dx.doi.org/10.1107/S0909049597013502
- [22] J. Verboncoeur, A. Langdon, and N. T. Gladd, "An object-oriented electromagnetic pic code," *Comp. Phys. Comm.*, vol. 87, pp. 199–211, May 1995.
- [23] K. Irikura, "Electron-impact cross section for ionization and excitation, nist standard reference database 107," 1997.
- [24] V. Vahedi and M. Surendra, "A monte carlo collision model for the particle-in-cell method: applications to argon and oxygen discharges," *Computer Physics Communications*, vol. 87, no. 1-2, pp. 179–198, may 1995.
- [25] J. Oberheide, P. Wilhelms, and M. Zimmer, "New results on the absolute ion detection efficiencies of a microchannel plate," *Measurement Science and Technology*, vol. 8, no. 4, p. 351, 1997. [Online]. Available: http://stacks.iop.org/0957-0233/8/i=4/a=001
- [26] N. Izumi, J. Emig, J. Moody, C. Middeleton, J. Holder, S. Glenn, T. Pond, R. Shellman, M. Cardenas, P. J. Walsh, S. J. Chelli, D. K. Bradley, and P. M. Bell, "Measurement of cathode luminescence efficiency of phosphors for micro-channel plate based x-ray framing cameras," in *Target Diagnostics Physics and Engineering for Inertial Confinement Fusion*, P. Bell and G. P. Grim, Eds. SPIE, oct 2012.
- [27] HAMAMATSU PHOTONICS K.K., "Direct image transmission fiber optic plates," Online, May 2013.
- [28] T. J. Dolan, "Magnetic electrostatic plasma confinement," Plasma Physics and Controlled Fusion, vol. 36, no. 10, p. 1539, 1994. [Online]. Available: http://stacks.iop.org/0741-3335/36/i=10/a=001
- [29] G.I.Dimov, I.S.Emelev, P.D.Vobly, V.V.Kobets, and M.A.Tiunov, "Multicusp Trap with Circular Geometry for Confinement of Low-Temperature Plasma," *Fusion Sci. Technol.*, vol. 59, pp. 211–213, 2011.
- [30] V. Belyaev, M. Dubrovin, P. Kosarev, A. Skovoroda, A. Spitsyn, A. Terent'ev, S. Yanchenkov, V. Zhil'tsov, and V. Zubarev, "Multicusp trap as model of plasma neutralizer for ITER neutral beam injector," *Fusion Science and Technology*, vol. 47, no. 17, pp. 124–127, jan 2005.
- [31] J. L. Pacheco, C. A. Ordonez, and D. L. Weathers, "Space-charge-based electrostatic plasma confinement involving relaxed plasma species," *Physics of Plasmas*, vol. 19, no. 10, p. 102510, oct 2012.
- [32] C. A. Ordonez, "Fully and partially non-neutral plasma equilibria in a variable-electrode-radius malmberg-penning trap," *Physical Review E*, vol. 67, no. 4, apr 2003.
- [33] R. E. Marrs, M. A. Levine, D. A. Knapp, and J. R. Henderson, "Measurement of electron-impact-excitation cross sections for very highly charged ions," *Physical Review Letters*, vol. 60, no. 17, pp. 1715–1718, apr 1988.
- [34] D. A. Dahl, "simion for the personal computer in reflection," *International Journal of Mass Spectrometry*, vol. 200, no. 1-3, pp. 3–25, dec 2000
- [35] M. A. Biondi and S. C. Brown, "Measurement of electron-ion recombination," *Physical Review*, vol. 76, no. 11, pp. 1697–1700, dec 1949.
- [36] H. Hus, F. Yousif, C. Noren, A. Sen, and J. B. A. Mitchell, "Dissociative recombination of electrons H₂⁺ in low vibrational states," *Physical Review Letters*, vol. 60, no. 11, pp. 1006–1009, mar 1988.
- [37] C. Bottcher, "Dissociative recombination of the hydrogen molecular ion," *Journal of Physics B: Atomic and Molecular Physics*, vol. 9, no. 16, pp. 2899–2921, nov 1976.
- [38] A. Jain, D. N. Gupta, and H. Suk, "Electron-ion recombination effect on electron acceleration by an intense laser pulse," *IEEE Transactions* on *Plasma Science*, vol. 47, no. 11, pp. 4891–4897, nov 2019.

VIII. FIGURES

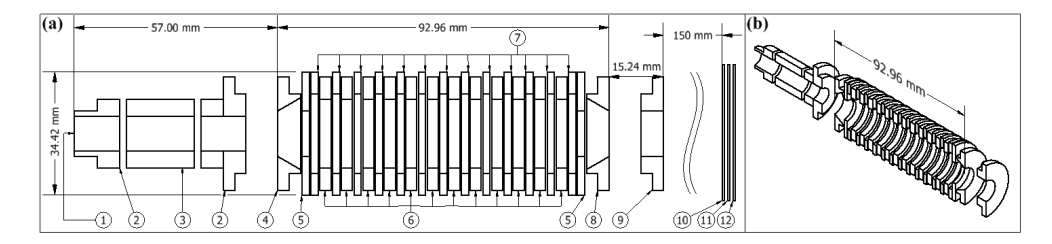


Figure 1. Scaled cross-section (a) and three-dimensional cutaway (b) of the einzel lens, space-charge-based ion trap, and MCP-PS assembly. The elements are: (1) Electron gun (not shown; arrow points to mount point and electron entry location). (2) Einzel lens grounded electrodes. (3) Einzel lens middle electrode. (4) and (8) Entrance and exit beveled elements. (5) Gate electrodes. (6) Permanent ring magnets. (7) Plugging electrodes. (9) Shielding electrode. (10) Front microchannel plate. (11) Back microchannel plate. (12) Phosphor screen. Note that elements (10-12) are not in scale with the rest of the drawing. Elements (2, 4, 5, 6, 9, front face of 11) are grounded. Elements (3, 8, back face of 11) have variable biases. Elements (7, front face of 10, 12) have fixed biases of -80 V, -1000 V, and 1800 V, respectively.

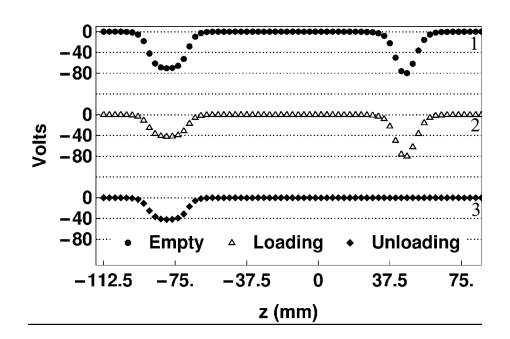


Figure 2. Electric potential along the axis of symmetry for different stages of operation, with the geometric center of the trap at z = 0. Voltages applied to the MCP-PS are not displayed. The axial potential profiles shown were computed without particles present using XOOPIC.

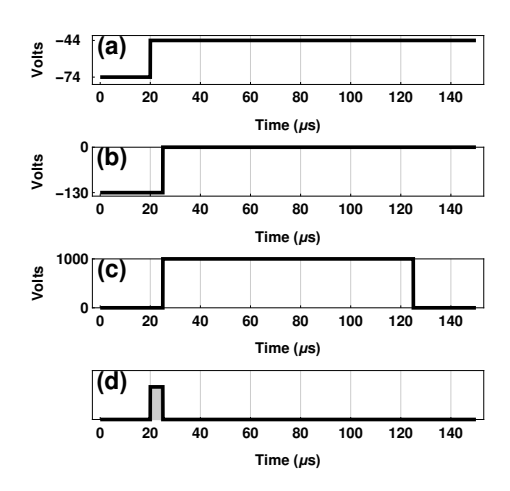


Figure 3. Electric pulses used for ion trapping. Plot (a) is the voltage applied to the middle einzel electrode, element (3) in Fig. 1. Plot (b) is the voltage on the beveled element at the exit, element (8) in Fig. 1. Plot (c) is the voltage applied to the back microchannel plate, element (12) in Fig. 1. Plot (d) shows the loading stage (shaded) during which charged particles build up inside the trap. In this figure the three stages of operation are defined as empty for t < 20 μs , loading for t < 20 t

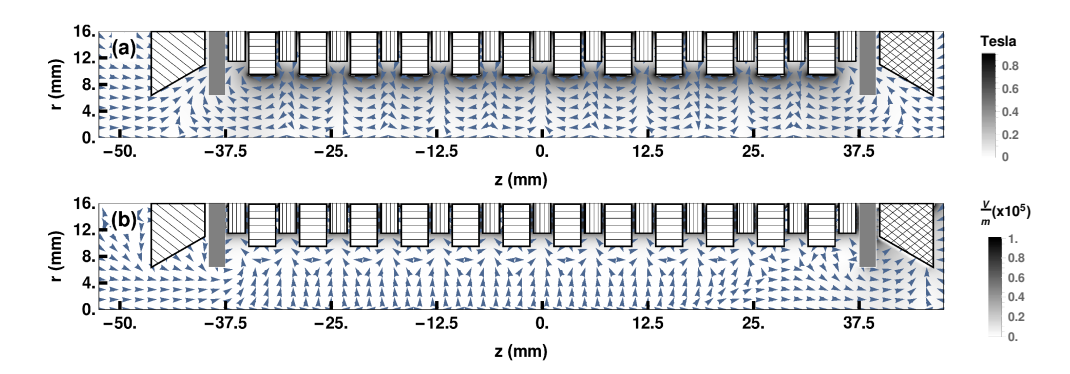


Figure 4. (a) Plots of the axisymmetric magnetostatic and (b) electrostatic vector fields and field magnitudes in the interior of the trap before the loading stage. The plugging electrodes (-80 V), magnets (0 V), gate electrodes (0 V), entrance beveled element (0 V), and exit beveled element (-130 V) are filled with vertical lines, horizontal lines, solid gray, diagonal lines, and crossed diagonal lines, respectively. The geometric center of the trap is at (r = 0, z = 0). Along the axis of symmetry (r = 0) the minimum magnetic field intensity is 0 T, at the trap's geometric center, and the nearest local maxima are .03 T at z = ± 3 mm. Along the axis of symmetry (r = 0) the electric field intensity is, $\sim 2 \text{ V/m} \pm 2 \text{ V/m}$, and ramps up to 7800 V/m at z = 40 mm.

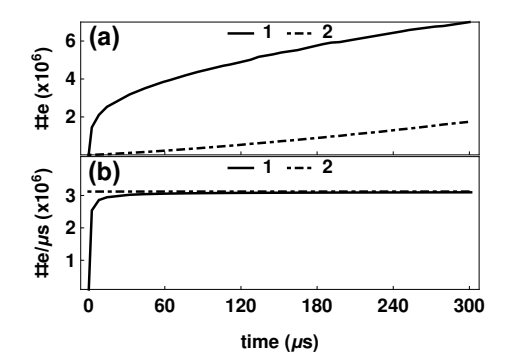


Figure 5. (a) Number of primary (curve 1) and secondary (curve 2) electrons in the trap. (b) primary electron loss rate (curve 1) compared to primary electron entry rate (curve 2).

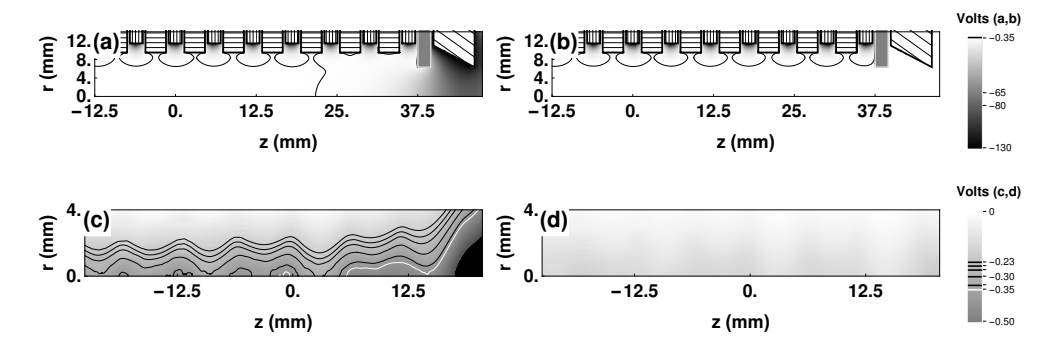


Figure 6. Axisymmetric plots of electric potential inside the trap. Shown are plots without charged particles present during (a) the loading stage and (b) the unloading stage. Plot (c) is at 32 μ s, with charged particles present during the loading stage. Plot (d) is at the end of a 36 μ s simulation, consisting of a 32 μ s simulation of the loading stage and an additional 4 μ s simulation of the unloading stage. In plot (c), black signifies that the electric potential is more negative than -0.5 V. The white contour line in plot (c) is along a potential of -.35 V. Such a potential value does not occur in plot (d). The geometric center of the trap is at (r = 0, z = 0).

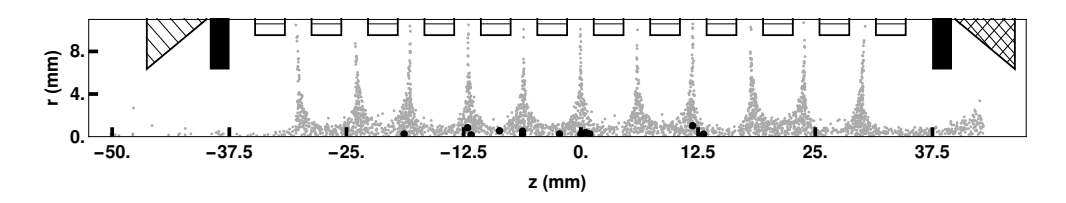


Figure 7. Positions of virtual electrons (gray dots) and confined virtual ions (black dots) at 32 μ s, for electric potentials corresponding to Fig. 6(c). The geometric shapes represent the corresponding elements in Fig. 4.

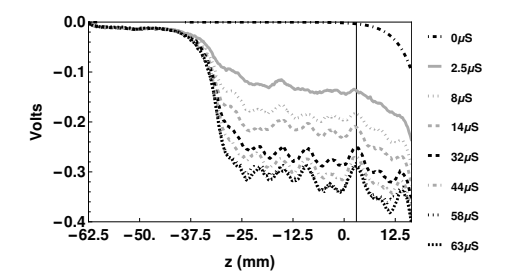


Figure 8. Electric potential along the z axis at eight different times during a simulation of the loading stage. The black vertical line marks the point with the highest potential on the axis inside the trap at $63 \mu s$.

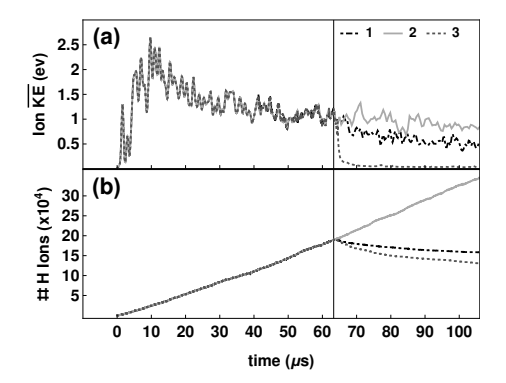


Figure 9. (a) Average kinetic energy of the total ion population and (b) total number of ions in the simulation. The vertical line marks the start (at 63 μ s) of three different second stages: continued loading (gray line, labeled 2); holding (dashed black line, labeled 1); and unloading (dashed gray line, labeled 3). (See text.)

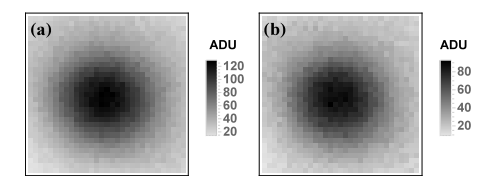


Figure 10. A signal image of the ROI at two pressures.

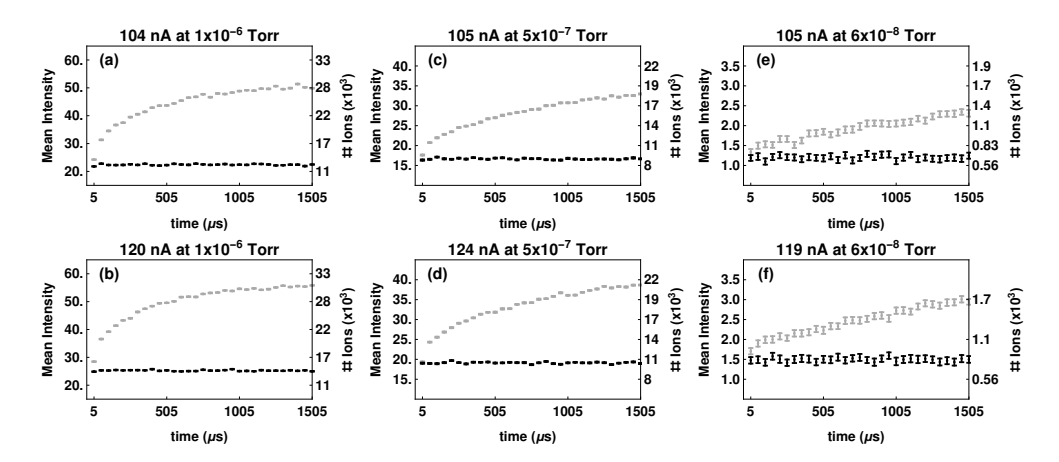


Figure 11. Experimentally acquired ion signals. The current and pressure labels are for convenience to aid in differentiating the various trials. The ion count on the right of each plot is an estimated value taken from the mean intensity in ADU $(1/1.62 \times ADU \times 900 \text{ pixels} = \text{total ions}$ in the ROI). The horizontal axis is the duration of the loading cycle prior to unloading the trap. Grey points are the signal of ions leaving the trap after an ion loading stage of increasing duration. Black points are the signal of ions leaving the trap with no loading stage. Included error bars are standard deviations across all images included in each data point. Each plotted point is the mean intensity value of the ROI for 50 images with identical loading times, except that 6×10^{-8} Torr trials had 100 images instead of 50.

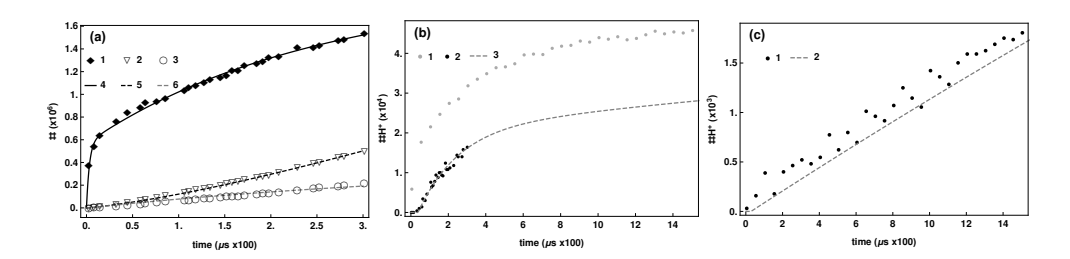


Figure 12. (a) Simulated primary electron population (marker 1), secondary electron population (marker 2), and free ion population (marker 3) located in the volume (3 mm \leq z \leq 14 mm, r < 6mm) in the trap compared to rate equation solutions for N_p (curve 4), N_s (curve 5), and N_u (curve 6) (Eqn. 1) for a background pressure of 1×10^{-6} Torr. (b) Measured ions (marker 1) (Fig. 11(b) black points subtracted from gray points) compared to simulated trapped ion population (marker 2) and the rate equation solution for N_i (curve 3). (c) Normalized measured ions (marker 1) for a background pressure of 6×10^{-8} Torr (Fig. 11(f) black points subtracted from gray points) compared to the pressure-scaled rate equation solution N_i discussed in the text. The range of the model parameter χ consistent with the data in (c) was used to estimate trapped ion lifetimes.